Science Advances
AAAS

advances.sciencemag.org/cgi/content/full/5/8/eaaw3203/DC1

Supplementary Materials for

Hydrophobic nanostructured wood membrane for thermally efficient distillation

Dianxun Hou, Tian Li, Xi Chen, Shuaiming He, Jiaqi Dai, Sohrab A. Mofid, Deyin Hou, Arpita Iddya, David Jassby, Ronggui Yang, Liangbing Hu*, Zhiyong Jason Ren*

*Corresponding author. Email: binghu@umd.edu (L.H.); zjren@princeton.edu (Z.J.R.)

Published 2 August 2019, *Sci. Adv.* **5**, eaaw3203 (2019)
DOI: 10.1126/sciadv.aaw3203

This PDF file includes:

Section S1. The hydrophobic silane treatment mechanism

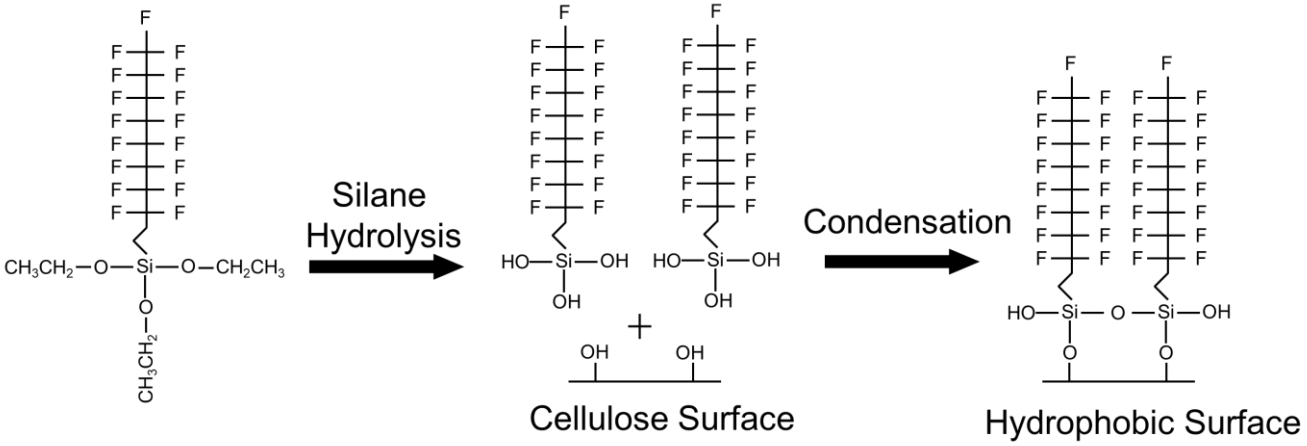

Fig. S1. Schematics of hydrophobic treatment of wood membranes using silane coupling agent (*50*).

Section S2. The nanowood membrane before and after hydrophobic treatment

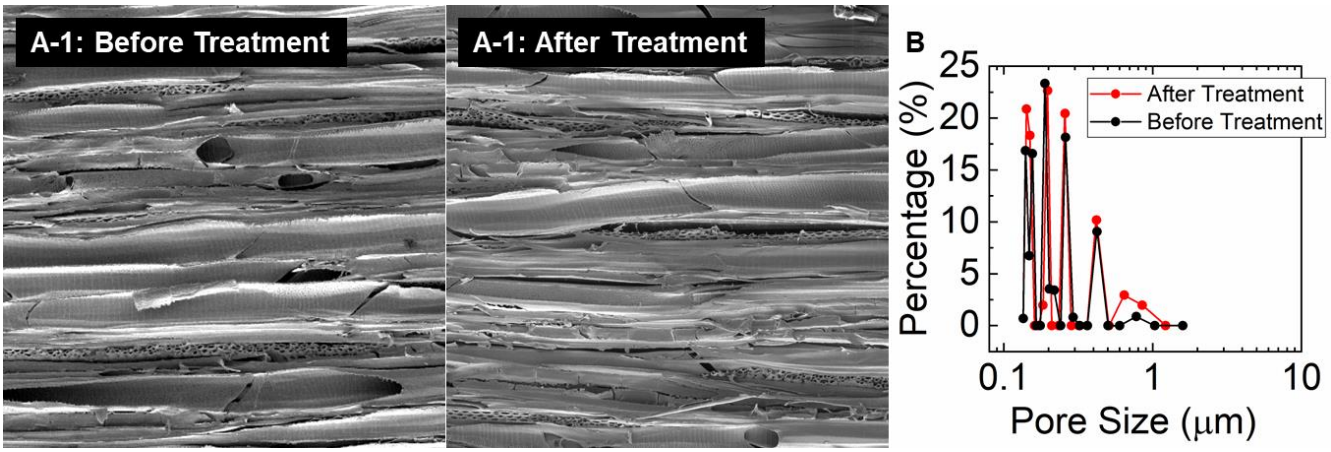

Fig. S2. Surface morphologies and pore size distribution of the nanowood membrane before and after hydrophobic treatment. (**A**) Surface morphologies and (**B**) pore size distribution of the nanowood membrane before and after hydrophobic treatment.

Section S3. The natural wood membranes

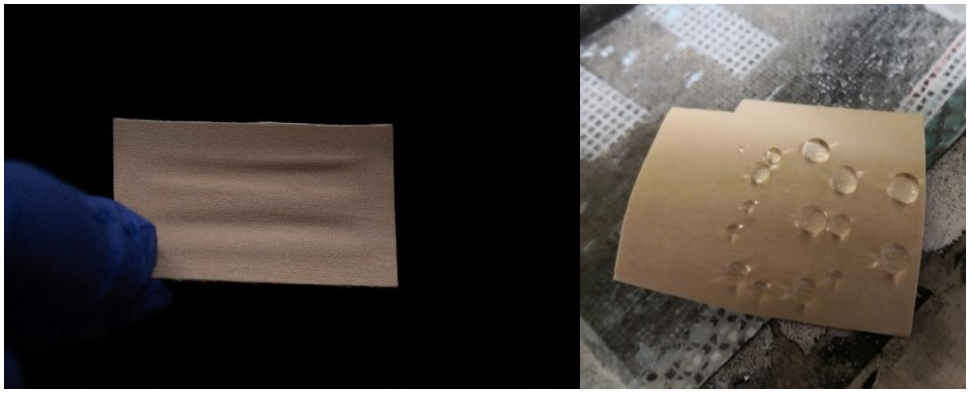

Fig. S3. Visual images of the hydrophobic natural wood membrane after silane treatment. Photo Credit: D. Hou, U. Colorado.

Section S4. Comparison of the wood membranes and common papers

Table S1. Comparison between nanowood and common paper.

	Nanowood Membrane	Paper
Mass density (g cm^{-3})	0.13	1.20
Mechanical (Tensile) strength (MPa)	18	0.25 – 0.30 (*41*)
Thermal conductivity (W m^{-1} k^{-1})	0.040	0.07 – 0.18 (*40*)
Fiber orientation	Aligned	Random
Anisotropic	Yes	No
Capability for bulk applications	Yes	No

Paper is one of the most widely used cellulosic products. During its manufacturing, wood chips were separated into cellulose fibers by removing the lignin from the wood, and the degraded cellulose fibers were then randomly mixed together to form an isotropic structure. This was deferent from the preparation of nanowood membrane, during which lignin and semi-cellulose fibers were removed via in situ chemical treatment and freeze-drying, allowing the preservation of the antistrophic microstructure and hierarchical alignment (Figure S4A, Figure 2A, Figure S2A). The different processing resulted in distinct properties between the paper and nanowood membrane. Credit to the large porosity of the hierarchical structure, the nanowood membrane demonstrated ~10 timer lower density (0.13 g cm^{-3}) than that of the paper (1.20 g cm^{-3}). Moreover, the alignment of cellulose nanofibers in nanowood with long chains resulted in high mechanical strength (18 MPa), while the mechanically and chemically degraded (broken) cellulose fibers with a random distribution in papers demonstrated a much lower mechanical strength (0.25-0.30 MPa). Furthermore, the higher porosity and aligned cellulose fibers granted the nanowood membrane anisotropic and super lower thermal conductivity.

Section S5. Anisotropic thermal insulation property of the nanowood membrane and the potential benefits

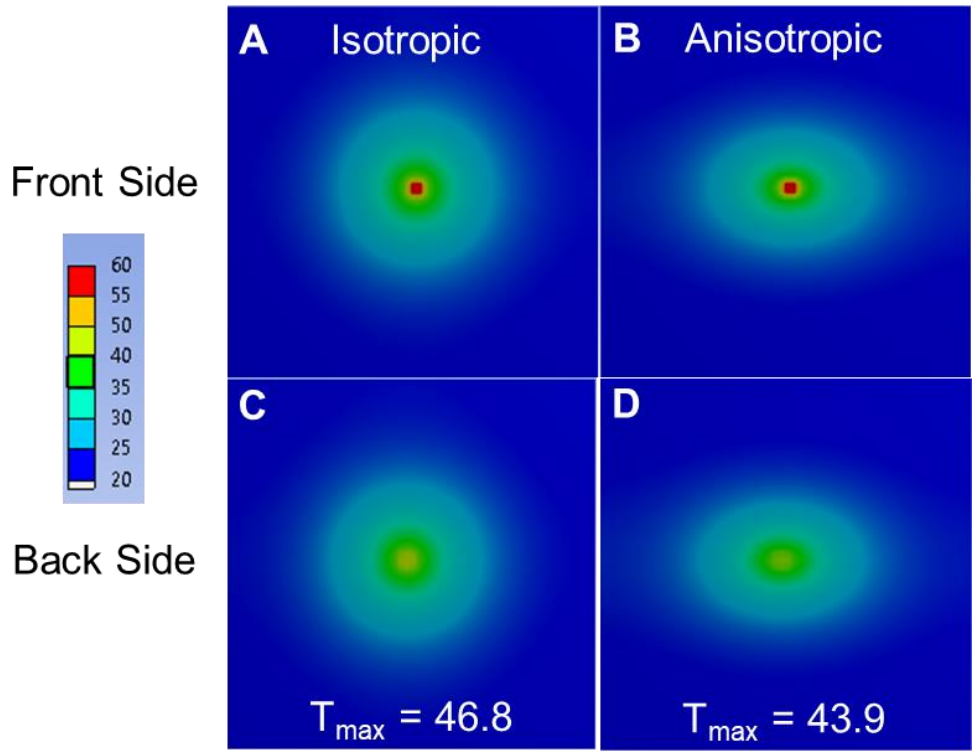

Fig. S4. Temperature plots of isotropic and anisotropic thermal insulators from a point heat source. (**A** and **B**) Front side surface temperature contour plot of the isotropic and anisotropic thermal insulators. (**C** and **D**) Back side surface temperature contour plot of the isotropic and anisotropic thermal insulators. The heat source on the top surface in the center was fixed at 60 ^{o}C. A natural convection boundary condition (ambient temperature of 22 ^{o}C, and convection heat transfer coefficient of 0.5 W m^{-2} k^{-1}) was applied to the peripheral surfaces. The isotropic thermal conductivity was 0.040 W m^{-1} k^{-1} (Table 1 and Section S12), while the anisotropic thermal conductivity in x-, y-, and z-direction were 0.060, 0.030 and 0.030 W m^{-1} k^{-1}, respectively (*39*). The modeled dimension was 40 mm (Width) × 40 mm (Height) × 0.502 mm (Thickness). Software: ANSYS 19.2 Academic.

Anisotropic Thermal Insulation Property of the Nanowood Membrane: When exposed to a local hot spot (60 ^{o}C), the isotropic thermal properties lead to an evenly distributed temperature contour profile with a circular shape on the front surface (Figure S5A). Credit to the hierarchical structure with aligned nanocellulose fibers (Figure 1), the nanowood membrane demonstrated an anisotropic thermal property, with an thermal conductivity in x-, y-, and z- direction is 0.060, 0.030 and 0.030 W m^{-1} k^{-1}, respectively (*39*). Heat can be easily transported in the x-direction (water flow direction in MD) due to directional high thermal conductivity, which yields an elliptical temperature distribution on the front surface (Figure S5B). The front-side temperature profiles were similar to those of the back-side temperature profiles. However, the low thermal conductivity in the traverse direction (vapor transport direction) together with heat dissipation along the aligned fibril direction with higher thermal conductivity of the nanowood prevented the conductive heat loss across the membrane.

The Potential Benefits: During MD, heat is continuously lost to the feed side through the membrane either via convective or conductive heat transfer, which led to a temperature gradient on the membrane surface in the water flow direction. Since monitoring the membrane surface temperature was difficult, we input our experimentally monitored temperatures (the temperatures of feed influent and effluent, and the temperatures of distillate influent and effluent), the obtained thermal conductivity and permeability coefficient back to a modified Schofield model (Section S14 in Supporting Information) to estimate the membrane surface temperatures at the feed inlet and outlet (*22*). Our modeling showed that at 60 ^{o}C, the temperature difference between the feed inlet and outlet points was ~0.8 ^{o}C for nanowood membrane, indicating a temperature gradient along the membrane surface on the feed side. Though the temperature gradient of 0.8 ^{o}C was not much in our experiment, it can be significant in a membrane module with a long flow channel. The anisotropic property of our nanowood membrane with improved thermal conductivity along the membrane surface (parallel to the fiber growth direction) was presumably to facilitate the heat transfer along the membrane thereby help maintaining the temperature gradient across the membrane and promote flux.

Section S6. Commercial hydrophobic membranes

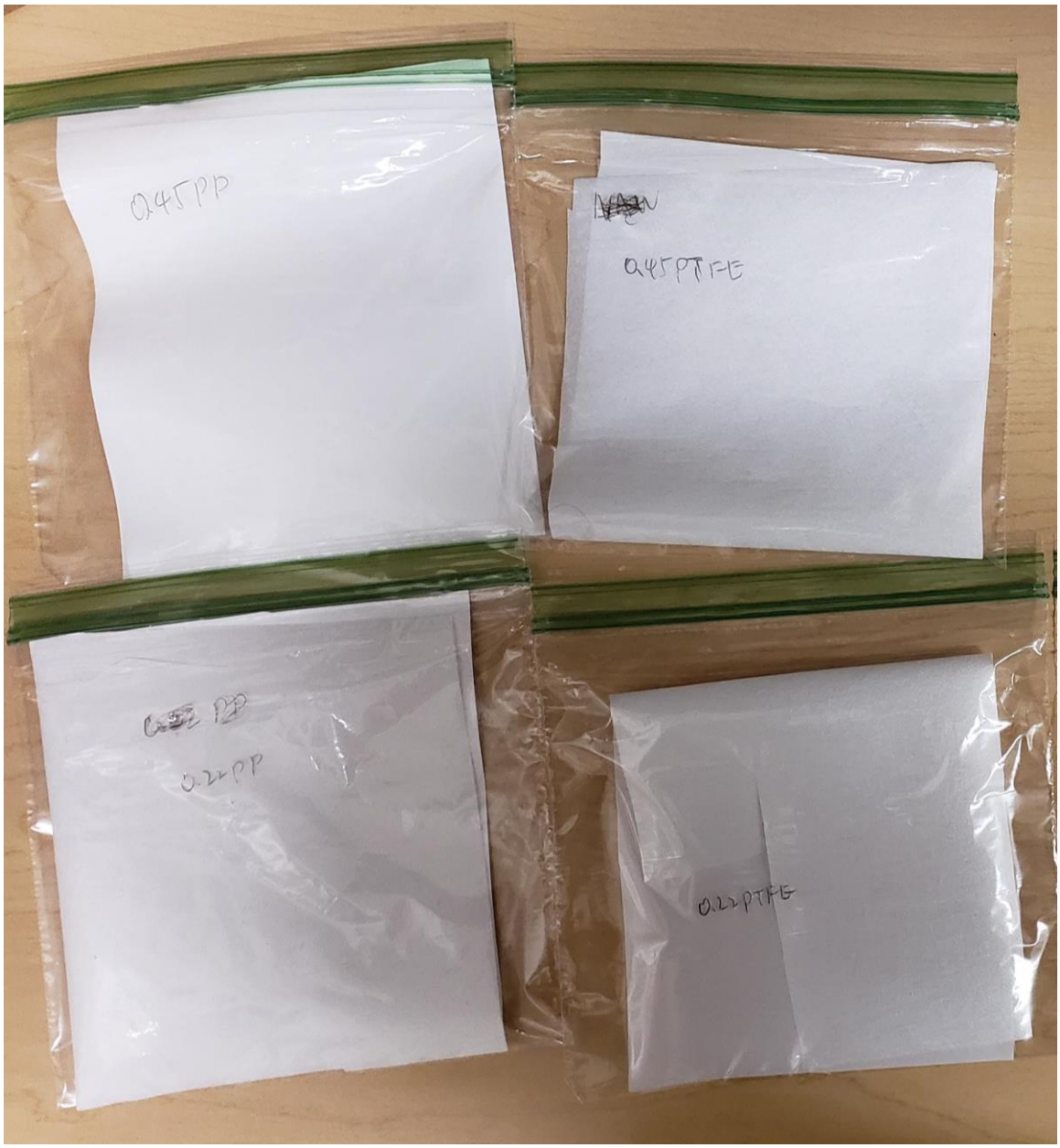

Fig. S5. Visual images of the commercial hydrophobic membranes purchased from Tisch Scientific (North Bend, Ohio).

Section S7. Pore size distribution of the commercial membranes

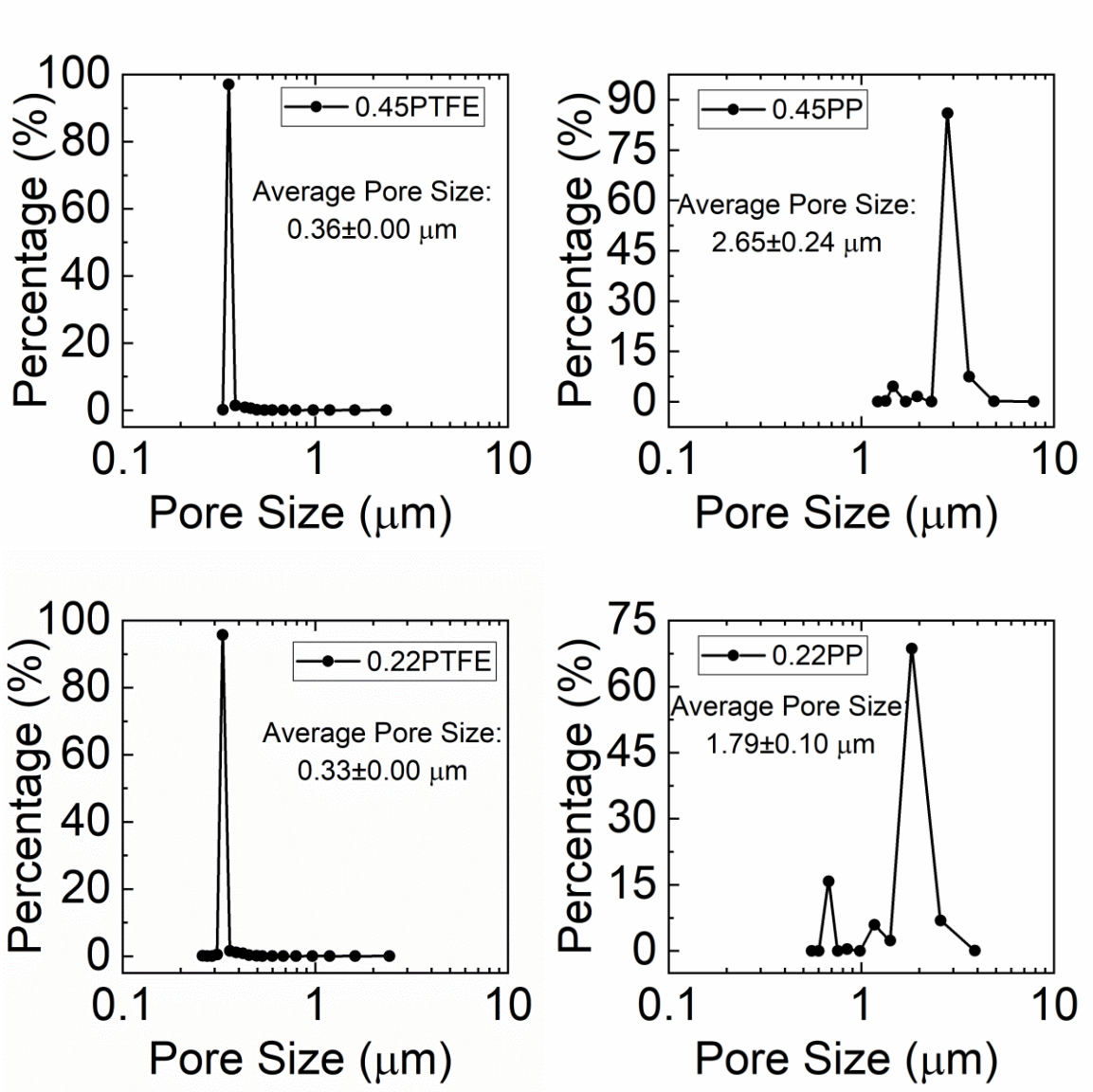

Fig. S6. PSD of the commercial membranes.

Section S8. Morphology and pore structure of the commercial membranes

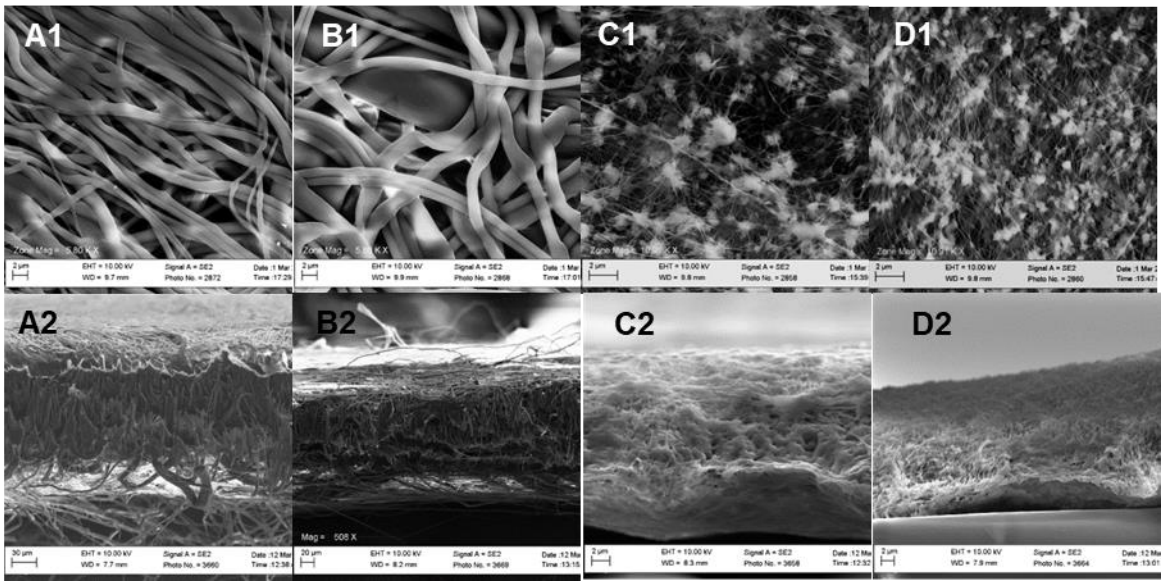

Fig. S7. SEM images of the surface and cross-section of the commercial membranes. SEM images of the surface (**1**) and cross-section (**2**) of the commercial membranes (**A**: 0.22PP, **B**: 0.45PP, **C**: 0.22 PTFE and **D**: 0.45PTFE).

Section S9. Surface hydrophobicity/hydrophilicity

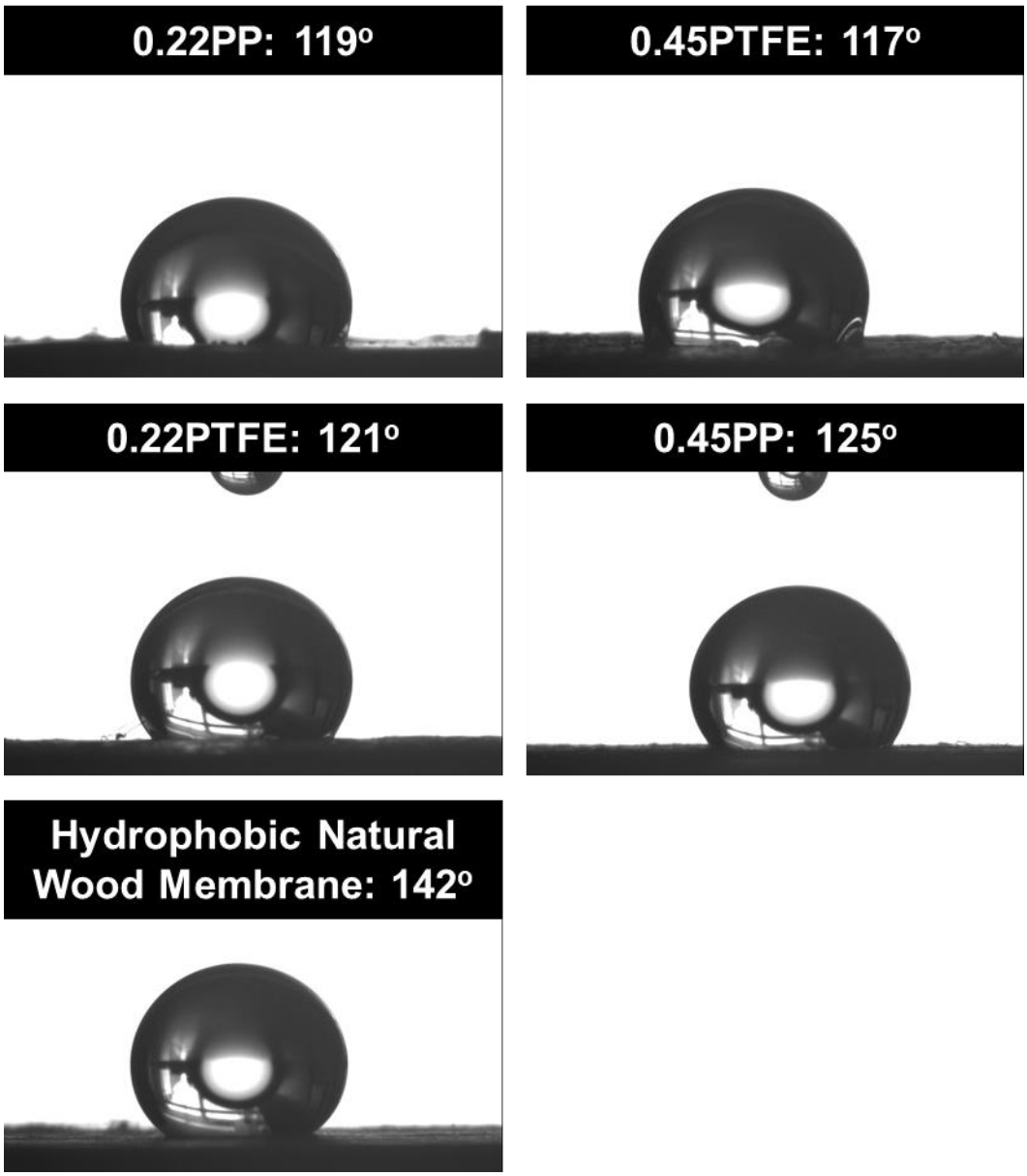

Fig. S8. Water contact angles of the commercial and hydrophobic natural wood membranes.

Section S10. DCMD reactors and configurations

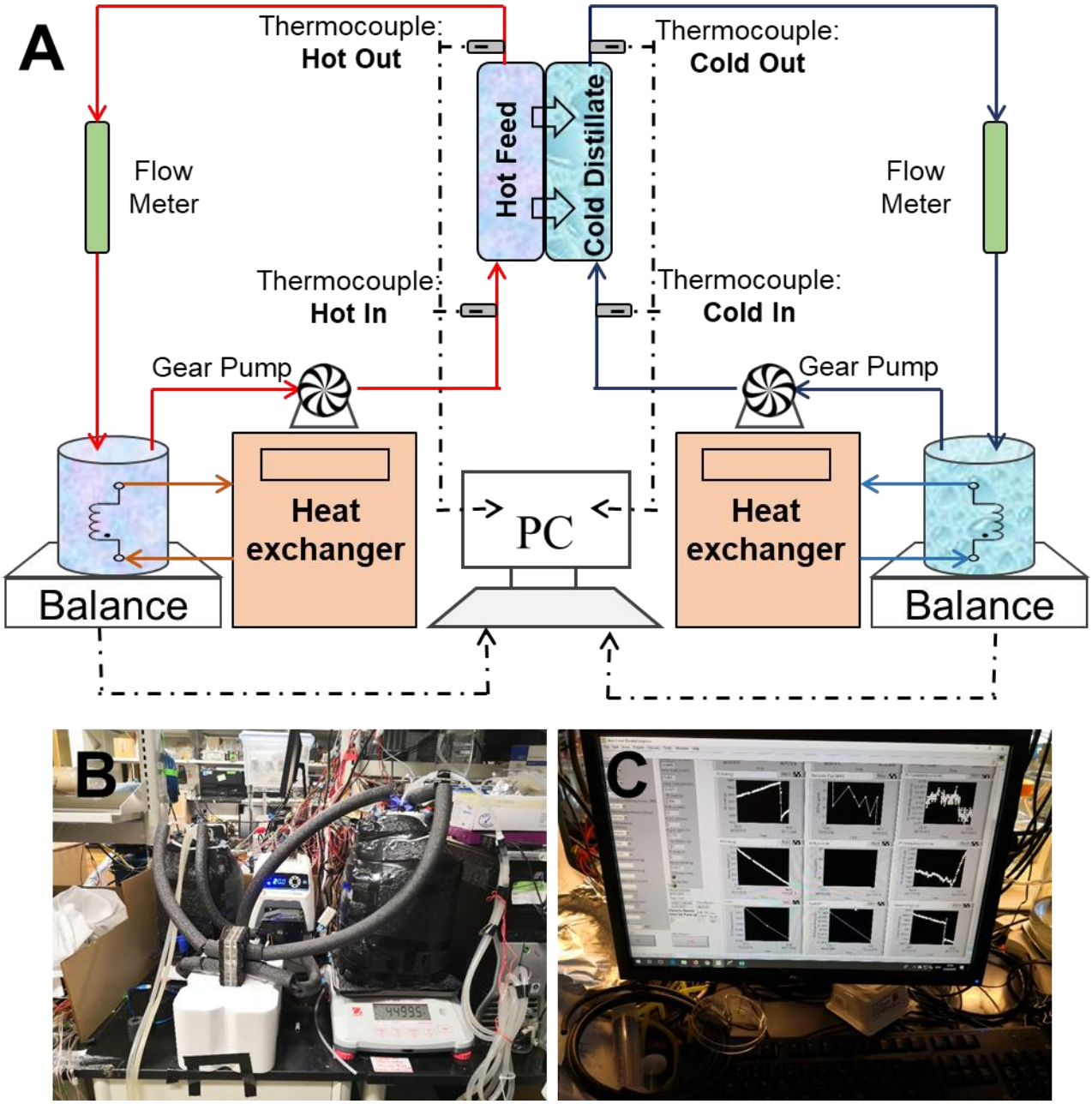

Fig. S9. Schematics, images, and control interface of the apparatus for direct contact membrane distillation (DCMD). (**A**) Schematics of the apparatus for direct contact membrane distillation (DCMD). Visual images of (**B**) the DCMD reactor and (**C**) LabVIEW control system. Photo Credit: D. Hou, U. Colorado.

Section S11. Water flux of commercial membranes

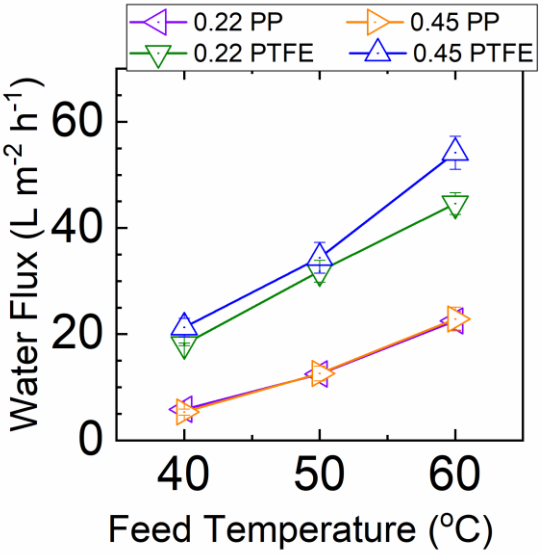

Fig. S10. Water flux of the commercial polymeric membranes in DCMD with feed [NaCl (1 g liter^{-1})] temperature continuously varying between 40° and 60°C and distillate (DI water) temperature of 20°C.

Section S12. Theoretical thermal conductivity estimation

The theoretical axial thermal conductivity of a membrane sample was estimated using a simple theoretical model (*59*),

$$\kappa_M = (1-\varphi)\kappa_m + \varphi\kappa_g \quad \text{Eq. S.1}$$

where φ is the porosity of membrane sample, κ_g is the thermal conductivity of gas, and κ_m is the thermal conductivity of the membrane material, respectively. For the commercial membranes with single phases, κ_g is the thermal conductivity of the materials, with PP and PTFE of 0.17 and 0.25 W m^{-1} K^{-1}, respectively. Since the wood membranes contain multiple phases, including cellulose (0.23 W m^{-1} K^{-1}), hemicellulose (0.34 W m^{-1} K^{-1}) and lignin (0.39 W m^{-1} K^{-1}), the material thermal conductivity was estimated according to their portions in the wood (*39, 47*).

The thermal conductivity of gas in the confined space nanofibrils can be estimated by (*39*),

$$\kappa_g = \frac{\kappa_{g,0}}{1+2\alpha l/D} \quad \text{Eq. S.2}$$

where $\kappa_{g,0}$ = 0.026 W m^{-1} K^{-1} is the thermal conductivity of gas in the free space, $\alpha \approx 2$ for air, l is the mean free path of gas and D is the mean pore size (Table 1). The mean free path of air is ~70 nm at ambient condition.

Section S13. Thermal insulation of commercial membranes

Due to the small thickness (< 200 μm), the thermal conductivity of the commercial membranes cannot be directly measured using LFA. Thus, we compared the insulating performance of the commercial membranes under the contact heat source at 60 ^{o}C (Figure S12). The backside temperatures of the PP and PTFE membranes were comparable, representing similar thermal insulation performance, which corresponded to the theoretical calculations (Section S12 and Table 1). With the verified theoretical thermal conductivity, we compared the insulating performance of the nanowood and commercial membranes at the same thickness (502 μm) using the ANSYS software with a point heat source of 60 ^{o}C (Figure S13). The backside maximum temperatures of the PP and PTFE membranes were comparable, representing similar thermal insulation performance. However, these were ~4 ^{o}C higher than that of the nanowood membrane, indicating that our nanowood membrane possessed much better thermal insulation property, which was due to its anisotropic property with reduced conductive heat transfer in the traverse direction (vapor transfer direction) and heat dissipation along the fiber growth direction (water flow direction).

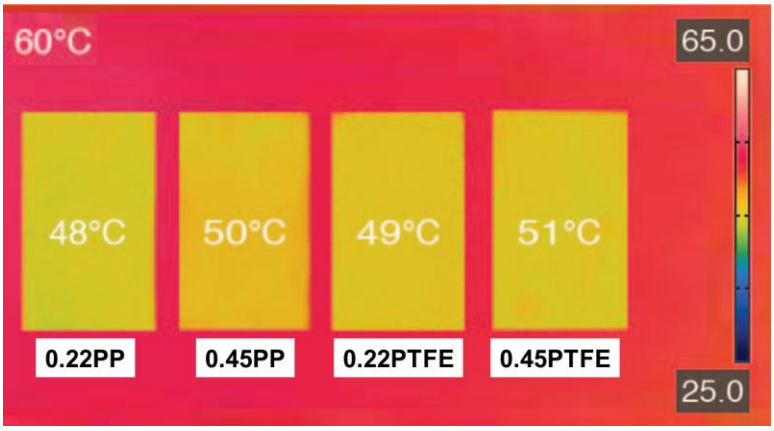

Fig. S11. IR thermographs of the commercial membranes with the heat source temperature of 60°C.

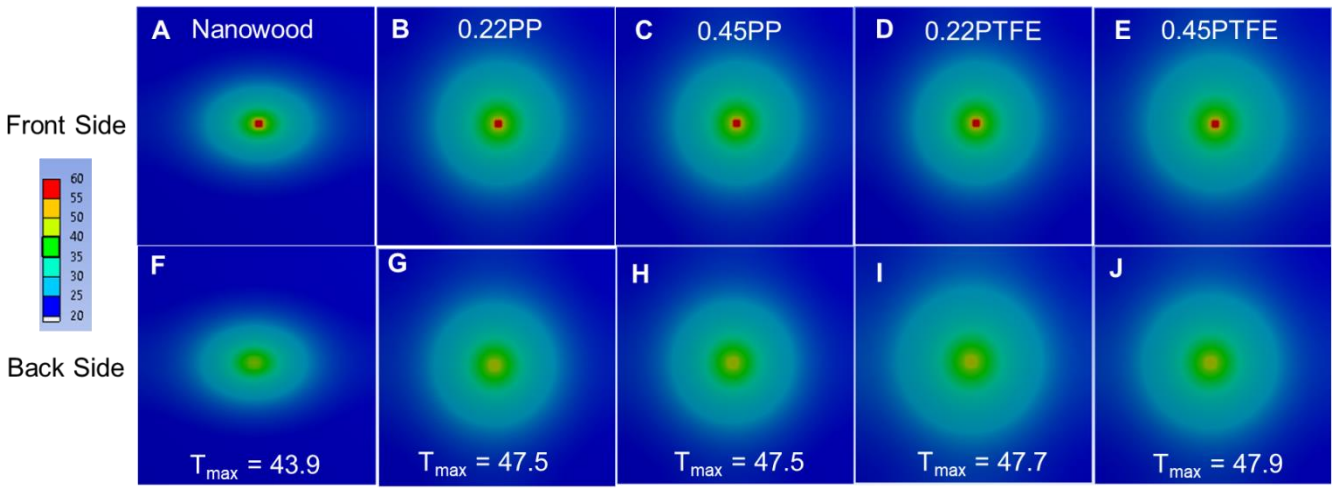

Fig. S12. Temperature plots of anisotropic nanowood and isotropic commercial membranes from a point heat source. Front side surface temperature contour plots (A to E) and the corresponding back side surface temperature contour plots (F and J). The heat source on the top surface in the center was fixed at 60 ^{o}C. A natural convection boundary condition (ambient temperature of 22 ^{o}C, and convection heat transfer coefficient of 0.5 W m^{-2} k^{-1}) was applied to the peripheral surfaces. The isotropic thermal conductivity for 0.22PP, 0.45PP, 0.22PTFE and 0.45PTFE were 0.066, 0.066, 0.082 and 0.075 W m^{-1} k^{-1}, respectively. The modeled dimension was 40 mm (Width) × 40 mm (Height) × 0.502 mm (Thickness).

Section S14. Experimental thermal conductivity and membrane permeability

In this research, we used a modified Schofield model to estimate the experimental thermal conductivity (*22*), along which we determined the water vapor permeability and intrinsic permeability (*23, 24*) of the wood and commercial membranes (Figure S15).

$$\frac{\Delta T}{J_v \beta} = \frac{1}{B_w \frac{dp}{dT} \beta} + \frac{1}{h \eta_{th}} \quad \text{Eq. S.3}$$

$$\beta = 2502800 + 2438.18 T_m \quad \text{Eq. S.4}$$

$$\frac{dp}{dT} = \frac{p_0 \beta}{R {T_m}^2} \quad \text{Eq. S.5}$$

$$p_0 = \exp(23.238 - \frac{3841}{T_m + 228.15}) \quad \text{Eq. S.6}$$

$$\eta_{th} = \frac{J_v A_m \beta}{(m_{d,in} + J_v A_m) C_{p,d,out} T_{d,out} - m_{d,in} C_{p,d,in} T_{d,in}} \quad \text{Eq. S.7}$$

Where ΔT is the bulk temperature difference, J_v the water flux, β the heat of vaporization of water (slightly dependent on temperature), B_w the membrane permeability coefficient, dp/dT the derivative to the temperature of the Antoine equation evaluated at the mean temperature of the membrane (T_m), h the total boundary layer heat transfer coefficient, η_{th} the thermal efficiency, p_0 the vapor pressure of pure water, and R the gas constant (8.314 m^3 Pa K^{-1} mol^{-1}), Am the membrane area, $m_{d,in}$ the mass flow rate of the distillate stream entering the distillate flow channel, $C_{p,d,in}$ the heat capacity of distillate influent, $C_{p,d,out}$ the heat capacity of distillate influent, $T_{d,out}$ the temperature of distillate effluent, and $T_{d,in}$ the temperature of distillate influent. Bw is obtained by interpolating the experimental data into Eq. S.3

Section S15. Theoretical permeability coefficient and intrinsic permeability

Transport of water vapor molecules from the bulk feed solution to the bulk permeate solution may be simulated using the widely-adopted "Dusty Gas Model" (DGM), which considered four different potential transport mechanisms through the membrane, including surface diffusion, viscous diffusion, molecular diffusion and Knudsen diffusion (*23*). Since MD membrane is hydrophobic, the surface diffusion resistance of water along membrane pores is high thereby considered negligible (*24*). Assuming a uniform pore size for a given MD membrane, a modified DGM equation considering viscous diffusion, molecular diffusion and Knudsen diffusion, is therefore employed:

$$B_w = B_{w,V} + B_{w,D} \qquad \text{Eq. S.8}$$

$$B_{w,v} = \frac{1}{8RT} \times \frac{\varepsilon r^2 P_{avg}}{\tau \delta \mu} \qquad \text{Eq. S.9}$$

where B_w is the theoretical membrane permeability coefficient (mol s kg^{-1} m^{-1}), $B_{w,V}$ viscous diffusion coefficient, $B_{w,D}$ is the combined Knudsen/ordinary diffusion coefficient. When the membrane pore diameter is between 0.5 and 50 times the length of the mean free path of water vapor (a pore-size range of 0.007 to 0.7 μm at 1 atm and 50 ^{o}C), Knudsen and molecular diffusion occur simultaneously (*23, 24*), thereby

$$B_w^D = \frac{B_w^K \times B_w^O}{B_w^K + B_w^O}\ Eq.10\ ;\ B_{w,K} = \frac{1}{RT} \times \frac{2\varepsilon r}{3\tau\delta} \times \sqrt{\frac{8RT}{\pi M}}\ Eq.11\ ; B_{w,O} = \frac{1}{RT} \times \frac{\varepsilon}{\tau\delta} \times \frac{PD}{P_{air}} Eq.12;$$

where $B_{w,K}$ is Knudesen diffusion coefficient, $B_{w,O}$ viscous diffusion coefficient, T the temperature (K), ε the membrane porosity, r the membrane pore size, τ the tortuosity (estimated as the inverse of porosity, 1/ε), δ the membrane thickness (m), M the molecular weight of water (0.018 kg mol^{-1}), P the total pressure inside the pore (Pa), D the diffusion coefficient of water vapor–air mixture (m^{-2} s^{-1}), P_{air} the air pressure in the pore (Pa). PD can be evaluated by an empirical formulas for the temperature range 273–373 K, given by (*58*),

$$PD = (1.895 \times 10^{-5})T^{2.072} \quad \text{Eq. S.13}$$

However, with smaller pore sizes (r < λ), Knudsen diffusion dominates, thus,

$$B_{w,D} = \frac{1}{RT} \times \frac{2\pi r^3}{3\tau\delta} \times \sqrt{\frac{8RT}{\pi M}} \quad \text{Eq. S.14}$$

While at larger pore sizes (r > 100λ), ordinary diffusion dominates, therefore,

$$B_{w,D} = \frac{1}{RT} \times \frac{\pi r^2}{\tau\delta} \times \frac{PD}{P_{air}} \quad \text{Eq. S.15}$$

The membrane permeability can be normalized with the membrane thickness to obtain the intrinsic membrane permeability (kg m^{-1} s^{-1} Pa^{-1}).

$$B_{w,I} = B_{w,I} \times M_{H2O} \times \delta \quad \text{Eq. S.16}$$

Where M_{H2O} is the molecular weight of water (kg mol^{-1}).

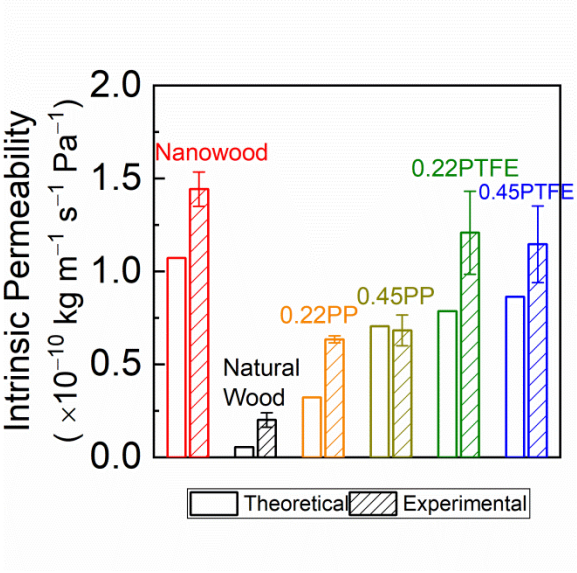

Fig. S13. Comparison of experimentally measured intrinsic (thickness-normalized) membrane permeability of the wood and commercial membranes. Membrane permeability modeled using DGM is typically lower than experimentally-measured permeability. Modeling condition: 1 g L^{-1} NaCl as feed solution (60 ^{o}C), DI water as distillate (20 ^{o}C).

Section S16. Wood membrane durability

The fabricated nanowood membranes demonstrated good stability in water flux and salt rejection in 6 hours DCMD experiment (Figure S16). After ~6 hours, water flux increased with salt rejection starting to decrease, which should be caused by membrane wetting. This is because the wood material is made of nanocellulose, which is extremely hydrophilic. Water vapor may be adsorbed by the non-fluorinated cellulose fibers during long term exposure, leading to wetting. However, the nanowood membrane can be fully restored by throughout rinsing using DI water and ethanol followed by drying at 120 °C for 4 h in a vacuum oven (-80 kPa). It is interesting to note that the natural wood membrane indicated better stability than the nanowood membrane under the experimental conditions, which might be attributed to its lower vapor flux thereby less vapor exposure as well as its better wetting resistance due to its smaller pore size and higher liquid entry pressure (Table 1). We believe that improved silane treatment without impact on the wood structure, such as adding silica nanoparticles, is needed to extend its longevity.

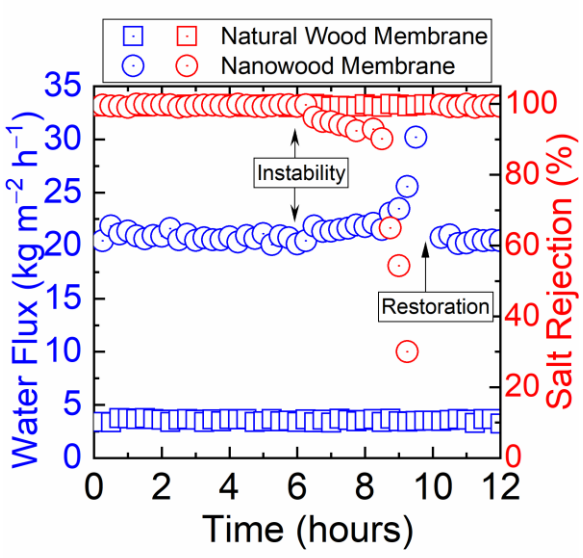

Fig. S14. Water flux of the hydrophobic wood membranes in DCMD with feed [NaCl (1 g liter^{-1})] and distillate (DI water) temperatures controlled at 60° and 20°C, respectively.

Section S17. Wood membrane application and fouling

MD is an emerging thermally driven process for desalination (*10*). Since the hydrophobic membrane blocks the passage of liquid water and the performance is less affected by the feed ionic strength, it shows great potential in treating highly contaminated and/or high-salinity streams, such as wastewater and seawater (*5, 6*). However, fouling may occur during the treatment of contaminated water containing foulants, which can result in the blocking of membrane pores, restriction of the passage of targeted resources, the degradation of the membrane material, and the need for frequent process disruptions designed to clean (physically and chemically) the membrane. So we investigated the fouling property of our nanowood membrane in treating synthetic seawater and wastewater (Figure S17). The synthetic seawater contained 35 g L^{-1} NaCl; and the synthetic wastewater contained 100 mg L^{-1} alginate, 75 mg L^{-1} humic acid, 25 mg L^{-1} BSA, 1.5 mM $CaCl_2$ and 6.0 mM NaCl, which were based on the secondary effluent quality in California. We operated the experiments for 5 hours and found the nanowood membrane showed stable flux in treating the synthetic seawater. However, the flux declined gradually when treating the synthetic wastewater, which should be due to membrane fouling caused by the strong hydrophobic-hydrophobic interactions between the membrane surface and hydrophobic domains present on natural organic matters (Figure 4A). The organic fouling can be exacerbated by the divalent ions (e.g., Ca^{2+} and Mg^{2+}) which promoted the coagulation of organic matters on the membrane surface. However, membrane fouling is affected by many factors, such as solution chemistry, temperature and flux, comprehensive studies should be carried out. Usually, the wetted or fouled hydrophobic membranes can be restored via rinsing or backwashing using water or chemicals, followed by drying. However, it is unclear how restoring membrane performance would impact the nanocellulose. Future work should explore the limits of nanowood durability under more extreme operating conditions, especially during chemical cleaning.

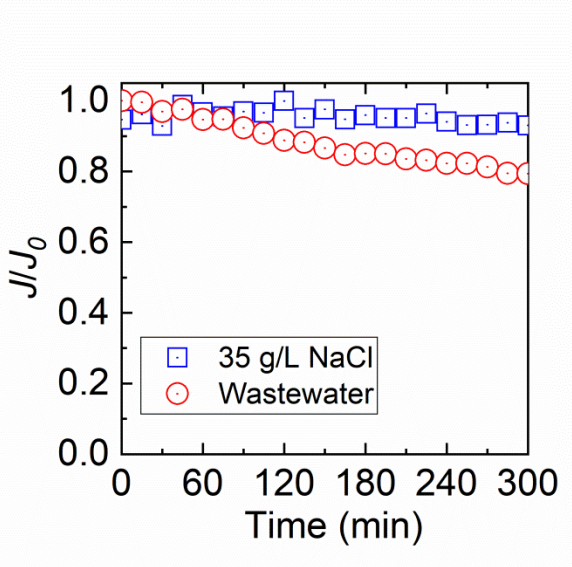

Fig. S15. Water flux of the hydrophobic nanowood membrane in DCMD with [NaCl (35 g liter^{-1}) and synthetic wastewater] and distillate (DI water) temperatures controlled at 60° and 20°C, respectively. The initial flux for 35 g L^{-1} NaCl and synthetic wastewater were 20.9 and 20.1 kg m^{-2} h^{-1}, respectively.